Vol. 4 • No. 16 • November 18 • 2014

www.advenergymat.de

ADVANCED ENERGY MATERIALS

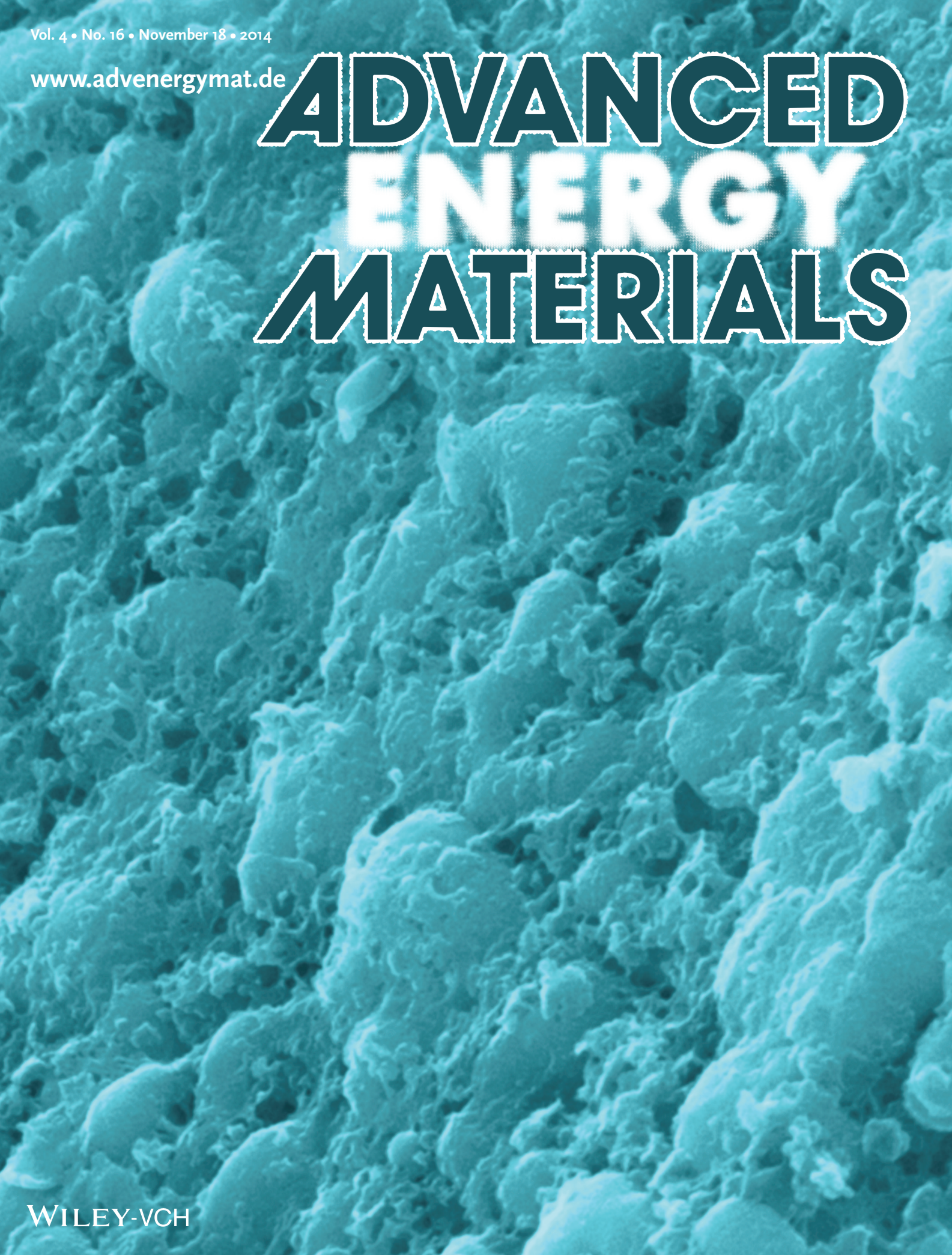

WILEY-VCH

ADVANCED ENERGY MATERIALS
www.advenergymat.de

Hierarchical Carbon Decorated $Li_3V_2(PO_4)_3$ as a Bicontinuous Cathode with High-Rate Capability and Broad Temperature Adaptability

*Yanzhu Luo, Xu Xu, Yuxiang Zhang, Yuqiang Pi, Yunlong Zhao, Xiaocong Tian, Qinyou An, Qiulong Wei, and Liqiang Mai**

Developing rechargeable lithium ion batteries with fast charge/discharge rate, high capacity and power, long lifespan, and broad temperature adaptability is still a significant challenge. In order to realize the fast and efficient transport of ions and electrons during the charging/discharging process, a 3D hierarchical carbon-decorated $Li_3V_2(PO_4)_3$ is designed and synthesized with a nanoscale amorphous carbon coating and a microscale carbon network. The Brunauer–Emmett–Teller (BET) surface area is 65.4 $m^2 g^{-1}$ and the porosity allows for easy access of the electrolyte to the active material. A specific capacity of 121 mAh g^{-1} (91% of the theoretical capacity) can be obtained at a rate up to 30 C. When cycled at a rate of 20 C, the capacity retention is 77% after 4000 cycles, corresponding to a capacity fading of 0.0065% per cycle. More importantly, the composite cathode shows excellent temperature adaptability. The specific discharge capacities can reach 130 mAh g^{-1} at 20 C and 60 °C, and 106 mAh g^{-1} at 5 C and –20 °C. The rate performance and broad temperature adaptability demonstrate that this hierarchical carbon-decorated $Li_3V_2(PO_4)_3$ is one of the most attractive cathodes for practical applications.

1. Introduction

To further prompt the development of electric vehicles, an electric battery with a fast charge/discharge rate, long lifespan and broad temperature adaptability is urgently needed.[1–11] Since the exploration reported by Nazar's group in 2002[12], monoclinic $Li_3V_2(PO_4)_3$ has attracted considerable interest as a commercial lithium ion battery cathode candidate because of its robust structure, high cell-voltage, thermal stability and fair theoretical specific capacity (197 mAh g^{-1} for complete extraction of three lithium ions when charged to 4.8 V, 133 mAh g^{-1} when cycled between the potential window of 3.0–4.3 V).[12–14] In particular, because of its sodium super ionic conductor (NASICON) structure, monoclinic $Li_3V_2(PO_4)_3$ provides a 3D pathway for Li^+ insertion/extraction, which results in a very high ion diffusion coefficient (from 10^{-9} to 10^{-10} cm^2 s^{-1}).[15–19] However, $Li_3V_2(PO_4)_3$ suffers a poor electronic conductivity (2.4×10^{-7} S cm^{-1} at room temperature) due to the nature of its separated VO_6 octahedral arrangement, which significantly limits its rate performance and the further commercialization.[20–24]

Carbon coating is an economic and feasible technique that is widely used to improve the electronic conductivity.[14,17,25–28] However, the common carbon coating could only provide an electron pathway on the nanoscale for individual particles. In comparison, the architecture combining the nanoscale carbon coating and the microscale carbon network could provide hierarchical pores for the electrolyte to pass through, which may supply a highly conductive network for both electrons and lithium ions, promoting the fast charge/discharge processes.[6,29–32] In addition, the fast kinetics enabled by this architecture would be beneficial for the battery performance at low temperature, which is a key issue in the application.

Here, we propose a feasible and environmentally friendly one-pot method utilizing glucose as both the carbon source and the reducing agent (functioned by the aldehyde group). Via the optimization of the interface reaction, hierarchical carbon (nanoscale amorphous carbon coating and microscale carbon network) decorated $Li_3V_2(PO_4)_3$ is obtained (Schematic, **Figure 1**). This unique architecture can provide the following three important features simultaneously: 1) continuous electron conduction enabled by hierarchical carbon, 2) rapid ion transport enabled by electrolyte-filled macro/mesopore network, and 3) a buffered protective carbon shell. The obtained cathode material achieved an enhanced rate capability (121 mAh g^{-1} at rate up to 30 C), superior cycling stability

Y. Z. Luo, X. Xu, Y. L. Zhao, X. C. Tian, Q. Y. An, Q. L. Wei, Prof. L. Q. Mai
State Key Laboratory of Advanced Technology for Materials Synthesis and Processing
WUT-Harvard Joint Nano Key Laboratory
Wuhan University of Technology
Wuhan 430070, P. R. China
E-mail: mlq@cmliris.harvard.edu; mlq518@whut.edu.cn
Y. X. Zhang, Y. Q. Pi
WUT Powerful Energy Co., Ltd
Wuhan 430223, P. R. China

DOI: 10.1002/aenm.201400107

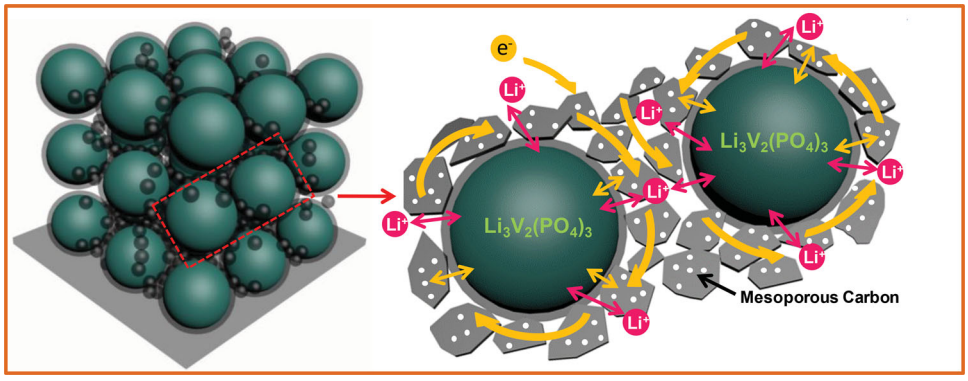

Figure 1. Schematic of hierarchical carbon decorated $Li_3V_2(PO_4)_3$ with pathways for both electrons and lithium ions.

(77% retention after 4000 cycles at the rate of 20 C) and excellent temperature adaptability (130 mAh g^{-1} at 20 C and 60 °C, 106 mAh g^{-1} at 5 C and –20 °C), indicating its superiority in practical applications.

2. Results and Discussion

The X-ray diffraction (XRD) patterns in **Figure 2**a show that the prepared $Li_3V_2(PO_4)_3$/C composites (LVP/C) are indexed to a monoclinic structure phase (JCPDS No. 01–072–7074) with a space group of $P2_1/n$, which is consistent with previous reports.[17,33,34] The composites are marked as LVP/C-1 to LVP/C-5 (molar ratio of $V_2O_5/H_2C_2O_4$ from 1:3 to 1:7). It is clear that all of the LVP/C samples are pure phase with no evidence of secondary phases or crystalline carbon diffraction peak.[33] The Raman spectrum of LVP/C-4 displays two characteristic bands of carbonaceous materials locating at 1318 cm^{-1} (D-band, disorder-induced phonon mode) and 1598 cm^{-1} (G-band, graphite band) (Figure 2b).[35] The value of the peak intensity ratio of the D to G band (I_D/I_G) is 0.98, indicating a relatively high degree of graphitization, which may result in an improved electronic conductivity.[15,36] However, the highly graphitized carbon exists without a long-range-ordering status, appearing as a very small and disordered state in the amorphous carbon. As a result, it is not able to detect any graphite crystallites from X-ray diffraction.[37]

The morphology of samples obtained by field emission scanning electron microscopy (FESEM) are shown in **Figure 3**a–c (LVP/C-4) and Supporting Information Figure S1. It is clear that the size of LVP particles is around 200–500 nm, which are embedded in the carbon matrix, with diameters of tens of micrometers. Energy-dispersive X-ray spectroscopy (EDS) results also show that the C, O, P and V elements is distributed uniformly in the final product (Supporting Information Figure S2). Moreover, the matrix is usually with one face covered by a thin carbon film that may act as a microscale current collector to facilitate the electron transport. The nanostructure of the LVP/C-4 particles is observed using transmission electron microscopy (TEM), which clearly shows the voids between the LVP/C particles. The high-resolution transmission electron microscopy (HRTEM) images (Figure 3d–f) show clear lattice fringes with d-spacings of 0.321 and 0.373 nm, which correspond to the (212) and (211) plane of monoclinic $Li_3V_2(PO_4)_3$, respectively.[17] The highly crystalline particle is coated with a thin amorphous carbon shell with the thickness of 2–3 nm. The pure carbon matrix was

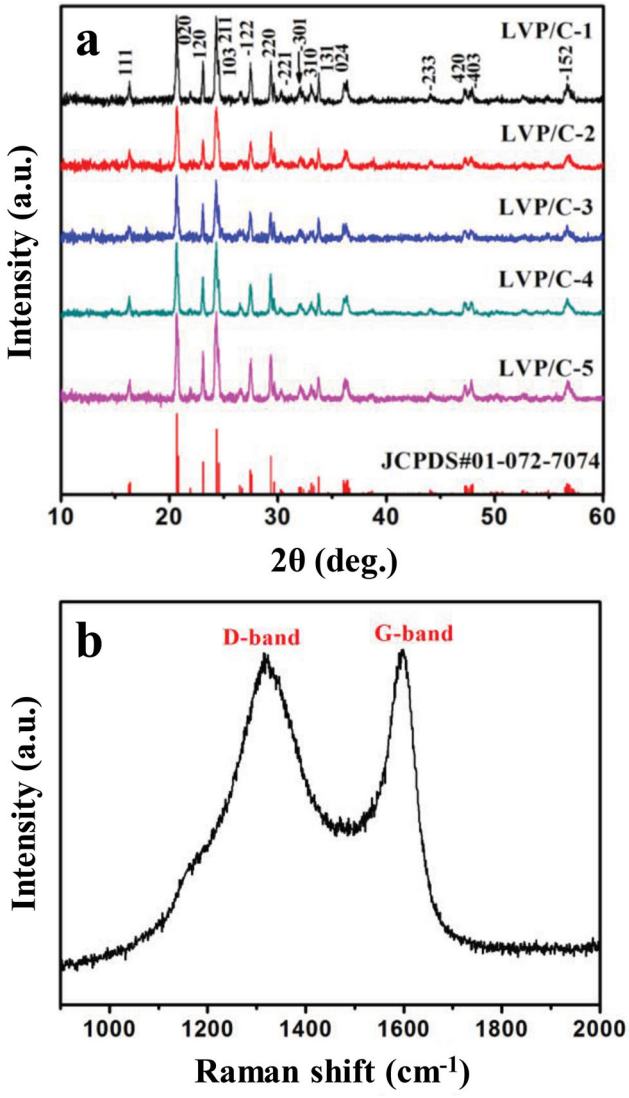

Figure 2. a) XRD patterns of the samples with different molar ratio of $V_2O_5/H_2C_2O_4$. b) Raman scattering spectrum of LVP/C-4.

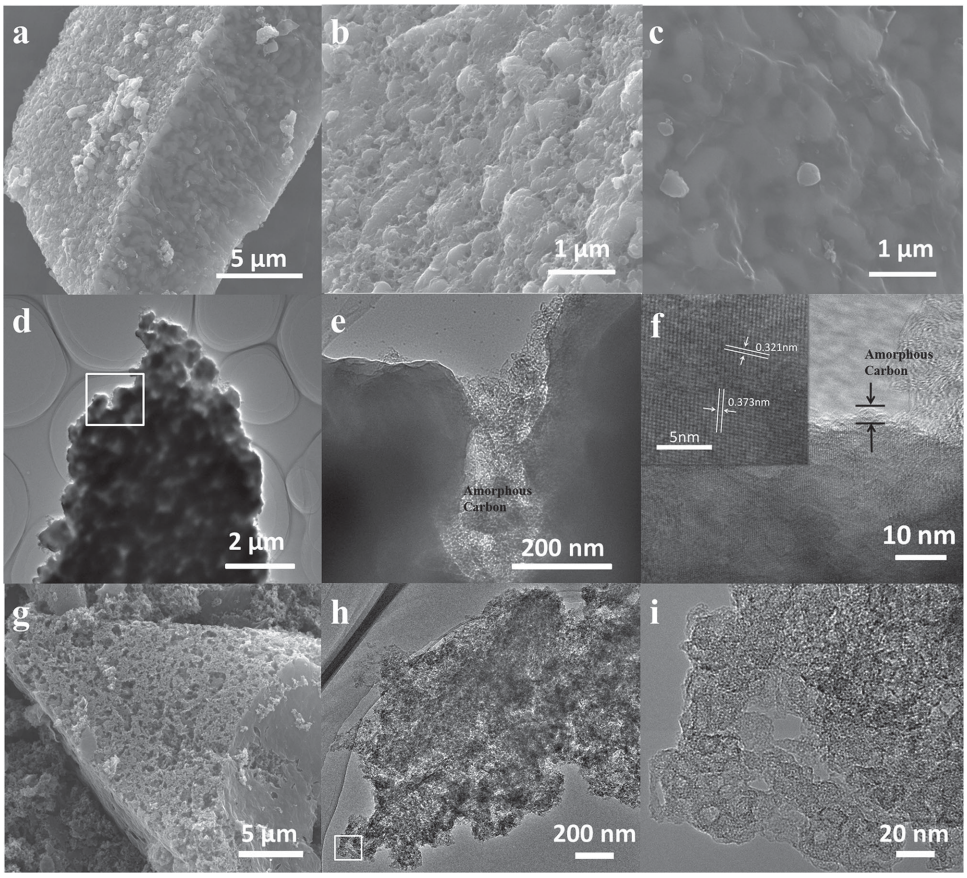

Figure 3. a–c) SEM and d–f) TEM images of LVP/C-4. g–i) SEM images of a pure carbon matrix after the corrosion of LVP particles. i) A magnified TEM image of the square area in (h).

also obtained via the corrosion of LVP/C-4 in the hydrofluoric acid solution to further confirm the 3D continuous carbon network (Figure 3g–i and Supporting Information Figure S3). The mesopores inside the matrix are clearly shown in the TEM images and Brunauer–Emmett–Teller (BET) isotherm exhibits a typical type-IV isotherm, which indicates the presence of a significant number of macropores (Supporting Information Figure S4). This carbon matrix with mesopores filled with the electrolyte is a conducting network for both electrons and lithium ions, which can make the $Li_3V_2(PO_4)_3$ particles more accessible to the electrolyte during the high-rate charge/discharge.[38]

The amount of oxalic acid has a great influence on the morphology of the final product. LVP/C-2, 3 and 5 have similar morphology with LVP/C-4. However, for LVP/C-1 sample, there is no carbon bridge between the particles (Supporting Information Figure S1). It is interesting that the samples LVP/C-1 to LVP/C-4 have similar BET surface areas of 65.3, 65.2, 61.1 and 65.4 $m^2\ g^{-1}$, respectively. The adsorption-desorption isotherms and the corresponding pore size distribution curves are shown in Supporting Information Figure S5. However, when the molar ratio of $V_2O_5/H_2C_2O_4$ changes to 1:7 for LVP/C-5, the SEM image clearly shows that the carbon particles between the LVP are too dense such that parts of the pores are blocked (Supporting Information Figure S1h), resulting in a much lower BET surface area of 49.7 $m^2\ g^{-1}$. The pore volumes of LVP/C-1 to LVP/C-5 are 0.186, 0.169, 0.182, 0.225 and 0.173 $cm^3\ g^{-1}$, respectively. According to the elemental analysis results, the amounts of carbon in the LVP/C-1 to LVP/C-5 are about 7.10%, 7.13%, 7.21%, 7.30% and 7.98%, respectively. In the synthesis process, glucose (aldehyde group) and oxalic acid can both as the reducing agents to reduce the VOC_2O_4. The following equations are involved.

$$V_2O_5 + 3H_2C_2O_4 \rightarrow 2VOC_2O_4 + 3H_2O + 2CO_2 \quad (1)$$

$$2C_6H_{12}O_6 + 4VOC_2O_4 + 3Li_2CO_3 + 6H_3PO_4 \rightarrow 2Li_3V_2(PO_4)_3 + 21H_2O + 7CO_2 + 6CO + 10C \quad (2)$$

$$2H_2C_2O_4 + 4VOC_2O_4 + 3Li_2CO_3 + 6H_3PO_4 \rightarrow 2Li_3V_2(PO_4)_3 + 11H_2O + 11CO_2 + 4CO \quad (3)$$

$$C_6H_{12}O_6 \rightarrow 6H_2O + 6C \quad (4)$$

For LVP/C-1, the $V_2O_5/H_2C_2O_4$ is 1:3, which means that oxalic acid is completely consumed to form vanadyl oxalate according to Equation (1). Therefore glucose is the only reducing agent to form $Li_3V_2(PO_4)_3$, as shown in Equation (2). Although LVP/C-1 has a similar carbon content to other samples, the carbon is mostly attached on the surface of the LVP

particles because of the full reaction of glucose as the reducing agent. For LVP/C-2 to LVP/C-5, there is extra oxalic acid, which may partly replace the glucose as the reducing agent, as shown in Equation (3). If the glucose acts as the reducing agent, the aldehyde group will be oxidized into carboxyl group and decomposes. Thus, one glucose molecule can decompose to five carbon molecules, which is one less than in Equation (4) if the glucose decomposes directly. As a result, with the increase of oxalic acid, the directly decomposed glucose increases, resulting in an increase in carbon content from LVP/C-1 to LVP/C-5. LVP/C-4 has a hierarchical carbon decorating structure, larger surface area and pore volume combined with suitable carbon content, which may contribute to better electrochemical performance.

Cyclic voltammetry (CV) results for the sample LVP/C-1, LVP/C-2, LVP/C-3, LVP/C-4 and LVP/C-5 are shown as **Figure 4**a. The voltammograms were measured at a scan rate of 0.1 mV s^{-1} in the potential range from 4.3 to 3.0 V vs Li/Li^+ at room temperature. All of these samples show the three pairs of anodic and cathodic peaks. It is obvious that the sample LVP/C-4 has the highest redox currents and largest curve area compared to the other samples. The sample LVP/C-4 is taken as an instance to explain the electrochemical process. The peaks around 3.61 and 3.70 V in the charge process present that the first lithium ion is extracted in two steps because of the existence of the ordered phases $Li_{2.5}V_2(PO_4)_3$ and $Li_2V_2(PO_4)_3$ with a mixed-valence V^{3+}/V^{4+}. The peak located at about 4.1 V is related to the delithiation of the second Li to form $LiV_2(PO_4)_3$, which corresponds to the complete oxidation of V^{3+} to V^{4+}.[39,40] The peaks at 3.51 V, 3.59 V and 4.0 V in the discharge process correspond to the reversible insertion of extracted lithium ions.

The battery performance of LVP/C samples was investigated against a Li foil. The constant current charging is followed by a potentiostatic hold at 4.3 V until the current drops to the one twentieth of charge current. The charge-discharge curves in Figure 4b all show three charge plateaus and three discharge plateaus. The three charge plateaus located around 3.60 V, 3.68 V and 4.08 V can be identified as the extraction of lithium ions and the corresponding phase transition processes during the electrochemical reactions. Meanwhile, during the discharge process, three plateaus located around 4.05 V, 3.65 V and 3.57 V can be attributed to the insertion of the extracted Li ions, which is accompanied by the phase transition from $LiV_2(PO_4)_3$ to $Li_3V_2(PO_4)_3$.

The initial discharge capacities and capacity retention of LVP/C samples after 100 cycles at different discharge rates (0.5, 2, 5, 10 and 20 C) are shown in Figure 4c. Compared with the theoretical discharge capacity of 133 mAh g^{-1} (3.0–4.3 V), the slight capacity loss might be due to the small quantity of carbon content in the cathode material.[41] It is obvious that LVP/C-4 shows more apparent superiority with the increasing rate. The detailed cycling performance of the samples at different rates is displayed in Supporting Information Figure S6. Compared with the sample without carbon, the superiority of LVP/C-4 is more obvious, especially at the high rate (Supporting Information Figure S7).

The detailed reaction kinetics of the LVP/C cathode material composite at the voltage of 3.60 V were investigated using electrochemical impedance spectroscopy (EIS) in the frequency range from 100 kHz to 0.01 Hz. All the Nyquist plots are composed of a small intercept in the highest frequency, two depressed semicircles at high and middle frequencies, combined with a slanted line in the low-frequency region (Supporting Information Figure S8). The resistance in the former semicircle can be attributed to the contact resistance between the LVP/C material and the current collector, while the latter indicates the charge-transfer resistance.[29] The slanted line in the low-frequency region corresponds to the ion diffusion.[42,43] The fitting result shows that the charge transfer resistances

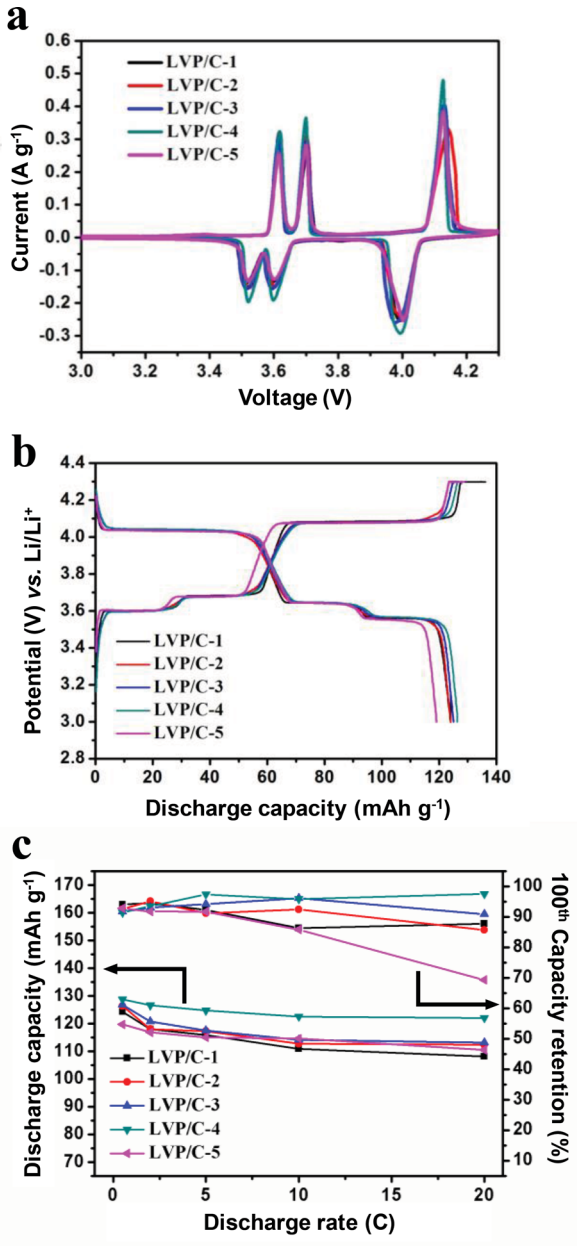

Figure 4. Electrochemical properties of LVP/C materials prepared with different molar ratios of $V_2O_5/H_2C_2O_4$. a) Cyclic voltammetry curves at a scan rate of 0.1 mV s^{-1} in the potential range from 4.3 to 3.0 V vs Li/Li^+. b) The second charge–discharge curves of LVP/C-1 to LVP/C-5 at 0.5 C. c) Comparison of the initial discharge capacities and capacity retention after 100 cycles versus different discharge rates.

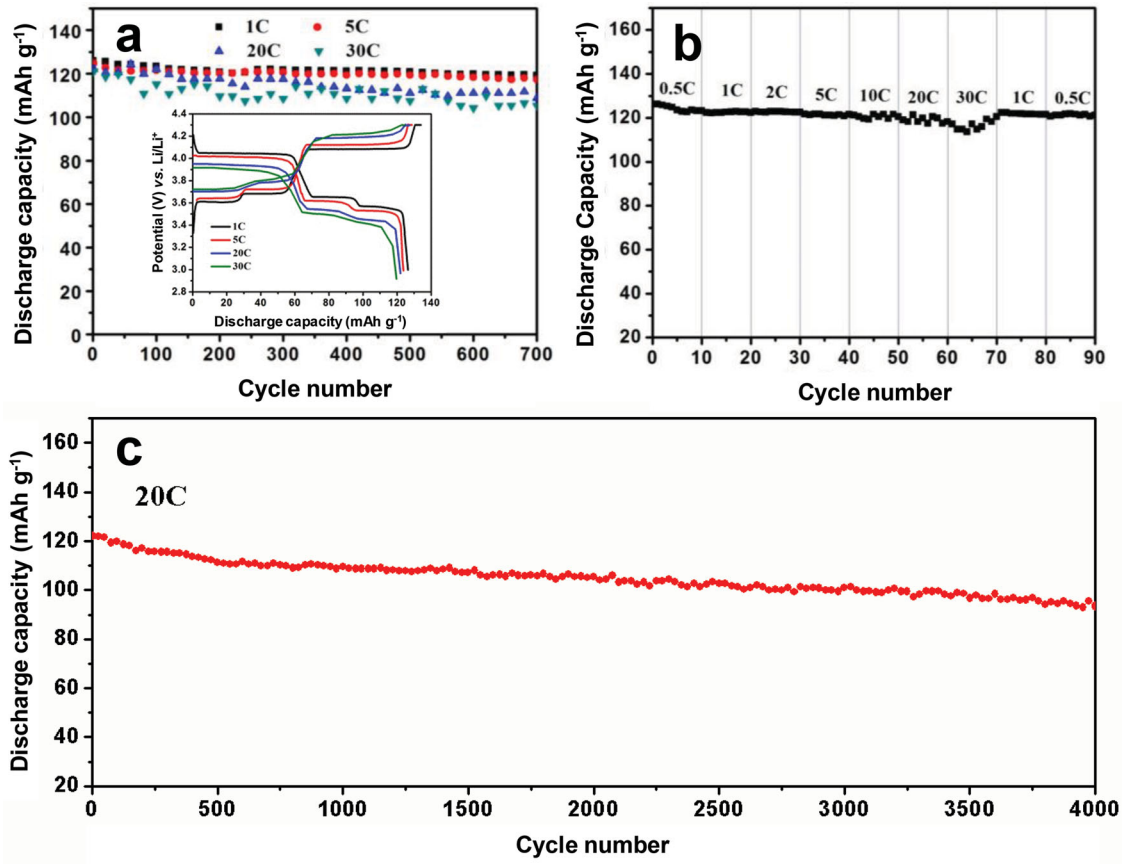

Figure 5. Electrochemical properties of LVP/C-4. a) The second charge–discharge curves (inset) and cycling performance at the current densities of 1, 5, 20 and 30 C, respectively. b) Discharge capacities of LVP/C-4 cathode at various rates from 0.5 C to 30 C. c) Charge–discharge cycling test of LVP/C-4 cathode at high rate of 20 C for 4000 cycles.

(R_{ct}) of the LVP/C samples before cycle are 71, 32, 34, 16 and 55 Ω, respectively. The values increase to 219, 94, 79, 41 and 141 Ω after the 10th cycle, respectively. The LVP/C-4 shows the lowest R_{ct} before cycle, and the increased R_{ct} after the 10th cycle is much smaller than other samples. The results demonstrate the superior interfacial stability of LVP/C-4, which is consistent with the cycling tests.

LVP/C-4 is found to have the best electrochemical performance, so it is chosen to investigate the high-rate and cycling performance. **Figure 5**a displays the cycling performance and the charge-discharge curves (inset) of LVP/C-4 at the rates of 1, 5, 20 and 30 C, respectively. With the increase in charge-discharge current density, the plateaus become shorter gradually. In addition, the problem of voltage rise/drop becomes more serious. Even then, the charge/discharge plateaus under the current density of 30 C are apparent. LVP/C-4 also shows excellent cycling stability at both high and low charge-discharge rate. When cycling at the rates of 1, 5, 20 and 30 C, it delivers capacities of 126, 124, 122 and 121 mAh g^{-1}, respectively. Remarkably, there are only small capacity decays of 7, 7, 13 and 16 mAh g^{-1} after 700 cycles, respectively. It is noteworthy that at 30 C rate, this 3D bicontinuous cathode still exhibited a capacity of 121 mAh g^{-1}, corresponding to 91% of the theoretical capacity, which indicates that the material displays low polarizations and good ionic diffusion rates.[44]

Figure 5b shows the rate performance of LVP/C-4 from 0.5 C to 30 C. It is clear that LVP/C-4 electrode exhibits a reasonably good cycling response at various current rates. Remarkably, even after 60 cycles, the capacity at the rate of 30 C can still reach 118 mAh g^{-1}. After this high rate measurement, the battery with LVP/C-4 cathode is able to supply the high capacity of 121 mAh g^{-1} at 1 C again. This performance demonstrates the advantage of our rationally designed 3D bicontinuous nanostructures, in addition to the excellent structural stability and the resulting high reversibility of LVP/C-4 cathode materials. Figure 5c displays the long-life performance of LVP/C-4 cathode. The initial specific discharge capacity is 122 mAh g^{-1} at the rate of 20 C. After 4000 cycles, the capacity is 94 mAh g^{-1}, corresponding to the capacity retention of 77% and capacity fading of 0.0065% per cycle.

In addition to high-rate and cycling performances, the temperature adaptability of this three-dimensional bicontinuous $Li_3V_2(PO_4)_3$/C cathode material was also investigated (**Figure 6**a,b). When measured under the temperature of 60 °C, it exhibits an initial capacity of 132 mAh g^{-1} at 5 C. Even after 400 cycles, the capacity of 120 mAh g^{-1} still remains. When the rate rises to 20 C, a high capacity of 130 mAh g^{-1} can be delivered for the first cycle and the capacity retention is 85% after 1000 cycles. In order to further explore the recover ability of LVP/C cathode material in temperature fluctuation, the

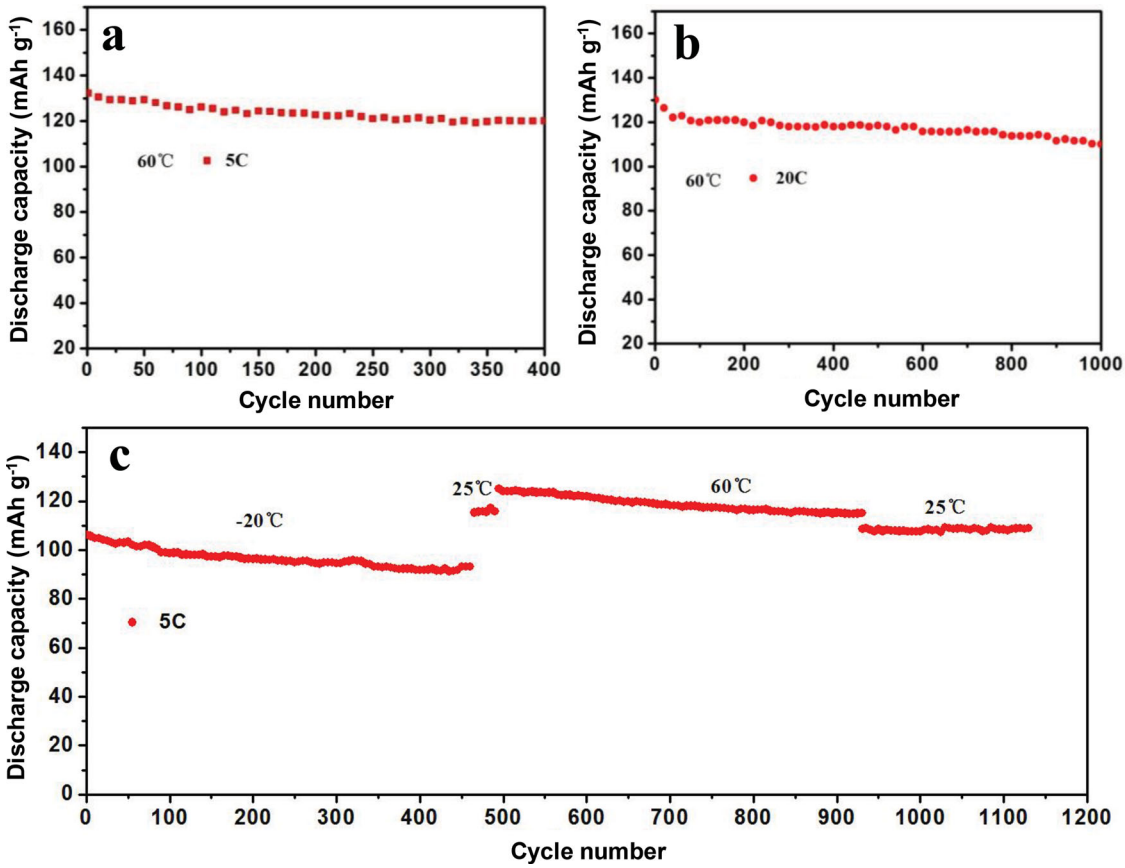

Figure 6. Electrochemical properties of LVP/C-4 at different temperatures. a) The cycling performance of LVP/C-4 on the temperature of 60 °C at rates of 5 C and b) 20 C. c) Discharge capacities of LVP/C-4 cathode at various temperatures from –20 °C to 60 °C at rate of 1 C charge and 5 C discharge.

recover test was carried out from –20 °C to 60 °C. Figure 6c shows the cycling performance between different temperatures at 5 C. When the half cell was operated at –20 °C, the cells were charged at 1 C and discharged at 5 C. While the cells were tested at 25 °C and 60 °C, the measurement was carried out at a 5 C charge/discharge rate. It can be seen that the reversible capacity progressively decreases at low temperature, which may be attributed to the slow diffusion of lithium ions. However, it still exhibits a high initial capacity of 106 mAh g^{-1} and capacity retention of 88% after 450 cycles at –20 °C. Then, the cell was heated back to 25 °C for the following tests. It is obvious that the discharge capacity can immediately return to 117 mAh g^{-1}. When the temperature increases to 60 °C, a high discharge capacity of 125 mAh g^{-1} can be obtained. Even when cycled under high and low temperatures hundreds of times, a discharge capacity of 108 mAh g^{-1} can still be obtained when the temperature decreased back to 25 °C.

Compared with the reported results, this material exhibits excellent high-low temperature performance with high capacity and outstanding cycling performance.[45–47] The unique hierarchical carbon-decorated structure is beneficial for both the high-temperature and low-temperature performance. First, the dissolution of the active materials at high temperature is efficiently suppressed because of the buffered protective carbon shell of the active material particles. Second, the slow kinetics at low temperatures are enhanced because of the 3D carbon network.

3. Conclusions

A 3D hierarchical carbon-decorated $Li_3V_2(PO_4)_3$ was designed and synthesized with a nanoscale amorphous carbon coating and a microscale carbon network. A specific capacity of 121 mAh g^{-1} can be obtained at the rate up to 30 C. When cycled at a rate of 20 C, the capacity retention is 77% after 4000 cycles, corresponding to a capacity fading of 0.0065% per cycle. More importantly, the LVP/C composite shows excellent temperature adaptability (130 mAh g^{-1} at 20 C and 60 °C, 106 mAh g^{-1} at 5 C and –20 °C). This outstanding high-rate performance and temperature adaptability may be attributed to the unique architecture, which provides the continuous electron conduction enabled by hierarchical carbon, rapid ion transport enabled by electrolyte-filled macro/mesopore network, and a buffered protective carbon shell of the active material particles. Our work indicates that this hierarchical carbon-decorated $Li_3V_2(PO_4)_3$ is one of the most attractive cathodes for practical applications.

4. Experimental Section

Synthesis of Carbon Decorated $Li_3V_2(PO_4)_3$: The material was synthesized by a sol–gel method combined with a conventional solid-state method. Different stoichiometric amounts of vanadium oxide (V_2O_5) and oxalic acid ($H_2C_2O_4$) were dissolved into distilled water with stirring at 80 °C for 15 min (molar ratio of $V_2O_5/H_2C_2O_4$ = 1:3, 1:4,

1:5, 1:6, 1:7). After the formation of transparent solution of VOC_2O_4, the phosphoric acid (H_3PO_4), lithium carbonate (Li_2CO_3) and glucose ($C_6H_{12}O_6$) were added into the above solution in order, to realize a molar ratio of Li:V:P:glucose = 3:2:3:1. The solution was stirred for 5 h to get a homogeneous precursor. Then, the precursor solution was dried at 120 °C in an air oven, followed by calcination at 350 °C for 5 h in nitrogen atmosphere to get a brown intermediate product. Finally, the brown powder was sintered at 800 °C for 8 h in nitrogen atmosphere to yield LVP/C material. The final products were marked as LVP/C-1 to LVP/C-5 (molar ratio of $V_2O_5/H_2C_2O_4$ from 1:3 to 1:7), respectively.

Characterization and Electrochemical Measurement: XRD measurements were performed to investigate the crystallographic information using a D8 Advance X-ray diffractometer with non-monochromated Cu Kα X-Ray source. FESEM images were collected with a JEOL JSM-7100F. TEM and HRTEM images were recorded by using a JEM-2100F STEM/EDS microscope. The specific surface area and pore size distribution was analyzed using Micromeritics Tristar 3020 instrument. C content analysis was determined by Vario EL cube CHNSO elemental analyzer. The property of carbon layer was analyzed with INVIA Raman Spectroscopy.

The electrochemical measurements were carried out by assembly of 2025 coin cells in a glove box filled with pure argon gas, which use lithium foil as the anode, 1 M solution of $LiPF_6$ in ethylene carbon (EC)/dimethyl carbonate (DMC) as electrolyte. Cathode electrodes were obtained with 70% $Li_3V_2(PO_4)_3$ material active material, 20% acetylene black and 10% poly(tetrafluoroethylene) (PTFE). The cells were aged for 12 h before charge/discharge to ensure full absorption of the electrolyte into the electrodes. The electrode area was 0.636 cm^2 (the disk with a diameter of 9 mm) and the mass loading of LVP/C was 4.72 mg cm^{-2}. Galvanostatic charge/discharge cycling was studied in a potential range of 4.3–3.0 V vs Li/Li^+ with a multichannel battery testing system (LAND CT2001A). The cells were charged under constant current and constant voltage (CCCV) mode, which was then discharged under constant current (CC) mode. The constant current charging is followed by a potentiostatic hold at 4.3 V until the current drops to one twentieth of charge current. The cells were then discharged to 3.0 V. CV was tested with an electrochemical workstation (CHI 760D). The AC impedance of each sample was analyzed using an Autolab PGSTAT 302N from 100 kHz to 0.01 Hz.

Supporting Information

Supporting Information is available from the Wiley Online Library or from the author.

Acknowledgements

Y.Z.L. and X.X. contributed equally to this work. This work was supported by the National Basic Research Program of China (2013CB934103, 2012CB933003), the International Science & Technology Cooperation Program of China (2013DFA50840), National Natural Science Foundation of China (51072153, 51272197) and the Fundamental Research Funds for the Central Universities (2014-yb-001). The authors thank Prof. C. M. Lieber of Harvard University and Prof. Dongyuan Zhao of Fudan University for strong support and stimulating discussions.
Note: this article was modified after online publication to improve the resolution of Figure 3.

Received: January 19, 2014
Revised: April 30, 2014
Published online: June 3, 2014

[1] M. Armand, J.-M. Tarascon, *Nature* **2008**, *451*, 652.
[2] J.-M. Tarascon, M. Armand, *Nature* **2001**, *414*, 359.
[3] A. S. Aricò, P. Bruce, B. Scrosati, J.-M. Tarascon, W. Van Schalkwijk, *Nat. Mater.* **2005**, *4*, 366.
[4] M. Yan, F. Wang, C. Han, X. Ma, X. Xu, Q. An, L. Xu, C. Niu, Y. Zhao, X. Tian, P. Hu, H. Wu, L. Mai, *J. Am. Chem. Soc.* **2013**, *135*, 18176.
[5] S. R. Gowda, V. Pushparaj, S. Herle, G. Girishkumar, J. G. Gordon, H. Gullapalli, X. Zhan, P. M. Ajayan, A. L. M. Reddy, *Nano Lett.* **2012**, *12*, 6060.
[6] L. Mai, Q. Wei, Q. An, X. Tian, Y. Zhao, X. Xu, L. Xu, L. Chang, Q. Zhang, *Adv. Mater.* **2013**, *25*, 2969.
[7] J. Liu, *Adv. Funct. Mater.* **2013**, *23*, 924.
[8] F. Cheng, J. Liang, Z. Tao, J. Chen, *Adv. Mater.* **2011**, *23*, 1695.
[9] N. Li, Z. Chen, W. Ren, F. Li, H.-M. Cheng, *Proc. Natl. Acad. Sci. USA* **2012**, *109*, 17360.
[10] N. Mahmood, C. Zhang, H. Yin, Y. Hou, *J. Mater. Chem. A* **2014**, *2*, 15.
[11] X. Wang, X. Cao, L. Bourgeois, H. Guan, S. Chen, Y. Zhong, D. M. Tang, H. Li, T. Zhai, L. Li, *Adv. Funct. Mater.* **2012**, *22*, 2682.
[12] H. Huang, S. C. Yin, T. Kerr, N. Taylor, L. F. Nazar, *Adv. Mater.* **2002**, *14*, 1525.
[13] J. Kim, J. K. Yoo, Y. S. Jung, K. Kang, *Adv. Energy Mater.* **2013**, *3*, 1004.
[14] J. Su, X.-L. Wu, J.-S. Lee, J. Kim, Y.-G. Guo, *J. Mater. Chem. A* **2013**, *1*, 2508.
[15] W. Duan, Z. Hu, K. Zhang, F. Cheng, Z. Tao, J. Chen, *Nanoscale* **2013**, *5*, 6485.
[16] S.-C. Yin, H. Grondey, P. Strobel, M. Anne, L. Nazar, *J. Am. Chem. Soc.* **2003**, *125*, 10402.
[17] C. Wang, H. Liu, W. Yang, *J. Mater. Chem.* **2012**, *22*, 5281.
[18] L.-L. Zhang, G. Liang, G. Peng, Y. Jiang, H. Fang, Y.-H. Huang, M. C. Croft, A. Ignatov, *Electrochim. Acta* **2013**, *108*, 182.
[19] X. Rui, N. Ding, J. Liu, C. Li, C. Chen, *Electrochim. Acta* **2010**, *55*, 2384.
[20] A. Pan, D. Choi, J.-G. Zhang, S. Liang, G. Cao, Z. Nie, B. W. Arey, J. Liu, *J. Power Sources* **2011**, *196*, 3646.
[21] A. Pan, J. Liu, J.-G. Zhang, W. Xu, G. Cao, Z. Nie, B. W. Arey, S. Liang, *Electrochem. Commun.* **2010**, *12*, 1674.
[22] A. Cho, J. Son, V. Aravindan, H. Kim, K. Kang, W. Yoon, W. Kim, Y. Lee, *J. Mater. Chem.* **2012**, *22*, 6556.
[23] H. Xiang, Z. Li, H. Wang, *J. Power Sources* **2012**, *203*, 121.
[24] Q. Chen, T. Zhang, X. Qiao, D. Li, J. Yang, *J. Power Sources* **2013**, *234*, 197.
[25] S. W. Oh, S. T. Myung, S. M. Oh, K. H. Oh, K. Amine, B. Scrosati, Y. K. Sun, *Adv. Mater.* **2010**, *22*, 4842.
[26] G. Wang, H. Liu, J. Liu, S. Qiao, G. M. Lu, P. Munroe, H. Ahn, *Adv. Mater.* **2010**, *22*, 4944.
[27] M. M. Ren, Z. Zhou, X. P. Gao, W. X. Peng, J. P. Wei, *J. Phys. Chem. C* **2008**, *112*, 5689.
[28] L. L. Zhang, G. Liang, G. Peng, Y. H. Huang, L. Wang, L. Qie, M. C. Croft, A. Ignatov, J. B. Goodenough, *J. Electrochem. Soc.* **2012**, *159*, A1573.
[29] H. Ji, L. Zhang, M. T. Pettes, H. Li, S. Chen, L. Shi, R. Piner, R. S. Ruoff, *Nano Lett.* **2012**, *12*, 2446.
[30] L. Mai, A. Minhas-Khan, X. Tian, K. Hercule, Y. Zhao, X. Lin, X. Xu, *Nat. Commun.* **2013**, *4*, 2923.
[31] L. Qie, W. Chen, H. Xu, X.-Q. Xiong, Y. Jiang, F. Zou, X. Hu, Y. Xin, Z. Zhang, Y. Huang, *Energy Environ. Sci.* **2013**, *6*, 2497.
[32] G. Zhou, D.-W. Wang, L. Li, N. Li, F. Li, H.-M. Cheng, *Nanoscale* **2013**, *5*, 1576.
[33] L. Mai, S. Li, Y. Dong, Y. Zhao, Y. Luo, H. Xu, *Nanoscale* **2013**, *5*, 4864.
[34] X. Rui, D. Sim, K. Wong, J. Zhu, W. Liu, C. Xu, H. Tan, N. Xiao, H. H. Hng, T. M. Lim, *J. Power Sources* **2012**, *214*, 171.
[35] T. Jiang, W. Pan, J. Wang, X. Bie, F. Du, Y. Wei, C. Wang, G. Chen, *Electrochim. Acta* **2010**, *55*, 3864.
[36] Y. Chen, D. Zhang, X. Bian, X. Bie, C. Wang, F. Du, M. Jang, G. Chen, Y. Wei, *Electrochim. Acta* **2012**, *79*, 95.

[37] L. Fei, W. Lu, L. Sun, J. Wang, J. Wei, H. L. Chan, Y. Wang, *RSC Adv.* **2013**, *3*, 1297.
[38] X. L. Wu, L. Y. Jiang, F. F. Cao, Y. G. Guo, L. J. Wan, *Adv. Mater.* **2009**, *21*, 2710.
[39] R. von Hagen, A. Lepcha, X. Song, W. Tyrra, S. Mathur, *Nano Energy* **2013**, *2*, 304.
[40] B. Pei, Z. Jiang, W. Zhang, Z. Yang, A. Manthiram, *J. Power Sources* **2013**, *239*, 475.
[41] H. Liu, P. Gao, J. Fang, G. Yang, *Chem. Commun.* **2011**, *47*, 9110.
[42] Y. Xu, Y. Zhu, Y. Liu, C. Wang, *Adv. Energy Mater.* **2013**, *3*, 128.
[43] X. L. Wu, Y. G. Guo, J. Su, J. W. Xiong, Y. L. Zhang, L. J. Wan, *Adv. Energy Mater.* **2013**, *3*, 1155.
[44] W. F. Mao, J. Yan, H. Xie, Z. Y. Tang, Q. Xu, *J. Power Sources* **2013**, *237*, 167.
[45] X. Rui, Y. Jin, X. Feng, L. Zhang, C. Chen, *J. Power Sources* **2011**, *196*, 2109.
[46] L. Zhang, S. Wang, D. Cai, P. Lian, X. Zhu, W. Yang, H. Wang, *Electrochim. Acta* **2013**, *91*, 108.
[47] Y. Qiao, J. Tu, X. Wang, C. Gu, *J. Power Sources* **2012**, *199*, 287.